PHYSICAL REVIEW B **106**, 014313 (2022)

Dynamical quantum phase transition in diamond: Applications in quantum metrology

Francisco J. González,[1] Ariel Norambuena,[1] and Raúl Coto[1,2,*]
[1]*Centro de Investigación DAiTA Lab, Facultad de Estudios Interdisciplinarios, Universidad Mayor, Chile*
[2]*Universidad Bernardo O Higgins, Santiago de Chile, Chile*

(Received 14 February 2022; revised 17 May 2022; accepted 15 July 2022; published 28 July 2022)

Nonequilibrium dynamics is a paramount scenario for studying quantum systems. The emergence of new features with no equilibrium counterpart, such as dynamical quantum phase transition (DQPT), has attracted wide attention. In this paper, we depart from the well-known Ising model and showcase an experimentally accessible configuration of a negatively charged nitrogen-vacancy center that interacts with nearby carbon-13 nuclear spins. We provide insights into this system in the context of DQPT. We show that nuclear spins undergo DQPT by appropriately choosing the relation between the transverse and longitudinal components of an external magnetic field. Furthermore, we can steer the DQPT via a time-dependent longitudinal magnetic field and apply this control to enhance the estimation of the coupling strength between the nuclear spins. Moreover, we propose a quenched dynamics that originates from the rotation of the central electron spin, which controls the DQPT relying on the anisotropy of the hyperfine coupling.

DOI: 10.1103/PhysRevB.106.014313

I. INTRODUCTION

Quantum phase transitions (QPT) rank among the most striking behavior of matter, in which a quantum system experiences a sudden change of its properties [1]. The variation of control parameters drives the system through a critical point where the free energy function becomes nonanalytic. In temperature-driven QPT, this point belongs to a critical temperature. However, QPT may happen even at zero temperature as quantum fluctuations drive the system's ground state. Furthermore, QPT can be susceptible to microscopic control parameters such as the atom-cavity detuning in Mott insulator-superfluid phase transitions [2,3]. In general, equilibrium QPT are well understood and provide a suitable path for unravelling the properties of a system [2–4]. In contrast, nonequilibrium QPT belong to an ongoing field that poses new challenges and opens new avenues to study QPT [5–8].

In recent years, nonequilibrium QPT have been studied in the context of physical quantities that become nonanalytic in time under quenched dynamics. This particular behavior has been termed as dynamical quantum phase transition (DQPT) [9]. Here, the time evolution resembles the effect of the driven parameter [6,9]. This idea has opened new horizons for theoretical studies about magnetization and entanglement [10], parameter estimation [11,12], as well as proof-of-principle experiments in trapped ions [10,13] and cold atoms [14]. The transverse-field Ising model is a paradigmatic system for the study of DQPT [9,10,15,16], however, this critical behavior has been observed in a wide variety of models [17–20]. Therefore, it is worth exploring configurations that lead to experimentally accessible devices in order to gain more insights and control of this phenomena.

The negatively charged nitrogen-vacancy (NV^-) center in diamond is a promising platform for quantum technologies [21,22]. The NV^- is an alternative to the well-established platforms of superconducting qubits, trapped ions, and cold atoms. It can be initialized, controlled, and read out with high fidelities. Moreover, it is stable at room temperature and exhibits long coherence time. It has delivered important applications in quantum information processing [23,24], quantum sensing [25–28], and quantum control [29–32]. Furthermore, it provides a testbed for different configurations of electron and nuclear spins [31,33,34].

In this paper we show that the NV^- can be used to control surrounding carbon-13 (^{13}C) nuclear spins to undergo DQPT. We extend the simulation of the well-known Ising model to consider dipolar interactions between ^{13}C and anisotropic coupling to the NV^-. Moreover, we consider an off-axis magnetic field to steer the DQPT. In addition, dynamical steering is allowed through a time-varying field, revealing new insights into the nonequilibrium dynamics of color centers in diamond. In this direction, we show that this particular dynamics can be harnessed to deliver a quantum sensing protocol. Furthermore, we show that after freezing the dynamics (both the magnetization and the rate function reach a steady state), backstage dynamics of quantum correlations provides a time window for maximally entangled states between the ^{13}C.

The paper is organized as follows. In Sec. II we introduce the system that is based on a NV^- interacting with nearby carbon-13 nuclear spins. In Sec. III we introduce DQPT, and we describe two different quenched dynamics, namely, quenched by external fields and quenched by a central spin. In Sec. IV we introduce a time-varying magnetic field to steer the DQPT. We apply this mechanism in quantum metrology to determine the coupling strength between two ^{13}C. Furthermore, we prepare a steady state for the magnetization and show that quantum correlations build up to create a maximally

---

[*] raul.coto@protonmail.com

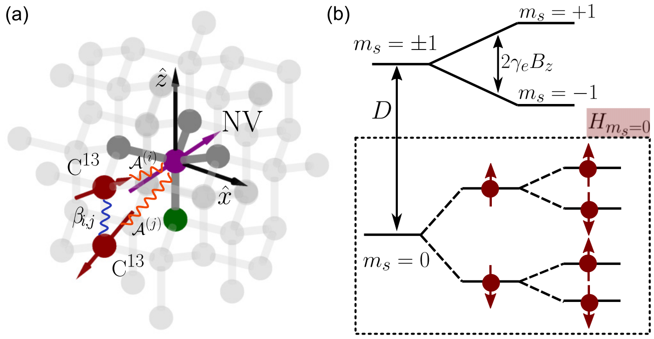

FIG. 1. (a) The NV$^-$ interacts with two ^{13}C nuclear spins in the diamond lattice. $\mathcal{A}^{(i)}$ is the hyperfine coupling tensor between the NV$^-$ and the ith nuclear spin. (b) Energy levels. The inset shows the splitting of the energy levels for the manifold $m_s = 0$ when the NV$^-$ interacts with two ^{13}C nuclear spins.

entangled state. In Sec. V we provide the final remarks of this paper.

II. SPINS CONFIGURATION

The negatively charged nitrogen-vacancy (NV$^-$) center in diamond is a point defect whose molecular structure is given by a substitutional nitrogen atom next to a vacancy in the crystal lattice. The NV$^-$ center has a C_{3v} symmetry and can be modeled as a two-electron hole system with spin $S = 1$. From *first-principles* calculations [35,36] based on dipole-dipole interaction of two electrons one obtains that the ground state of this defect presents a natural zero-field splitting $D/2\pi = 2.87$ GHz between $m_s = 0$ and $m_s = \pm 1$ degenerated states [37,38]. Hence, an external magnetic field along the N-V axis (symmetry axis) lifts the degeneracy between states $m_s = \pm 1$ because of the Zeeman effect. In addition, full control of the spin triplet can be addressed by a microwave field [37]. Nearby spin-1/2 ($I = 1/2$) carbon-13 (^{13}C) nuclear spins are hyperfine coupled to the NV$^-$. Moreover, each ^{13}C interacts with the nuclear spins bath via dipolar interaction, as shown in Fig. 1. The Hamiltonian of the system reads

$$\hat{H} = D\hat{S}_z^2 + \gamma_e \mathbf{B}\cdot\mathbf{S} + \mathbf{S}\cdot\sum_{i=1}^{N}\mathcal{A}^{(i)}\cdot\mathbf{I}^{(i)} + \hat{H}_I, \tag{1}$$

where $\gamma_e/2\pi = 2.8$ MHz/G is the gyromagnetic ratio of the electron spin and $\mathbf{B} = B_x\hat{x} + B_z\hat{z}$ corresponds to the external magnetic field. The B_x component will be used for external control of the dynamics of the whole system. $\mathcal{A}^{(i)}$ is the hyperfine tensor, and $\hat{H}_I$ is the Hamiltonian of nuclear spins that is given by

$$\hat{H}_I = \gamma_n \mathbf{B}\cdot\sum_{i=1}^{N}\mathbf{I}^{(i)} + \hat{H}_n, \tag{2}$$

where $\gamma_n/2\pi = 1.07$ kHz/G is the gyromagnetic ratio of the ^{13}C and $\mathbf{I}^{(i)}$ is the nuclear spin operator of the ith ^{13}C. $\hat{H}_n$ corresponds to the dipole interaction between the nuclear spins that is written as

$$\hat{H}_n = \sum_{i<j}\frac{\mu_0\gamma_n^2}{4\pi r_{ij}^3}\left(\mathbf{I}^{(i)}\cdot\mathbf{I}^{(j)} - \frac{3(\mathbf{I}^{(i)}\cdot\mathbf{r}_{ij})(\mathbf{r}_{ij}\cdot\mathbf{I}^{(j)})}{r_{ij}^2}\right), \tag{3}$$

with μ_0 the vacuum permeability, and r_{ij} is the distance between the ith and jth nuclear spins. The vector $\mathbf{r}_{ij}$ in spherical coordinates reads $\mathbf{r}_{ij} = (r_{ij}^x, r_{ij}^y, r_{ij}^z) = (r_{ij}\sin\theta_{ij}\cos\phi_{ij}, r_{ij}\sin\theta_{ij}\sin\phi_{ij}, r_{ij}\cos\theta_{ij})$. Thereby, the Hamiltonian for the nuclear interaction is written as

$$\hat{H}_n = \sum_{i<j}\frac{\mu_0\gamma_n^2}{4\pi r_{ij}^3}[\hat{A}_{ij} + \hat{B}_{ij} + \hat{C}_{ij} + \hat{D}_{ij} + \hat{E}_{ij} + \hat{F}_{ij}], \tag{4}$$

with

$$\begin{aligned}
\hat{A}_{ij} &= \hat{I}_z^{(i)}\hat{I}_z^{(j)}(1 - 3\cos^2\theta_{ij}),\\
\hat{B}_{ij} &= -\tfrac{1}{4}\big[\hat{I}_+^{(i)}\hat{I}_-^{(j)} + \hat{I}_-^{(i)}\hat{I}_+^{(j)}\big](1 - 3\cos^2\theta_{ij}),\\
\hat{C}_{ij} &= -\tfrac{3}{2}\big[\hat{I}_+^{(i)}\hat{I}_z^{(j)} + \hat{I}_z^{(i)}\hat{I}_+^{(j)}\big]\sin\theta_{ij}\cos\theta_{ij}e^{-i\phi_{ij}},\\
\hat{D}_{ij} &= -\tfrac{3}{2}\big[\hat{I}_-^{(i)}\hat{I}_z^{(j)} + \hat{I}_z^{(i)}\hat{I}_-^{(j)}\big]\sin\theta_{ij}\cos\theta_{ij}e^{i\phi_{ij}},\\
\hat{E}_{ij} &= -\tfrac{3}{4}\hat{I}_+^{(i)}\hat{I}_+^{(j)}\sin^2\theta_{ij}e^{-2i\phi_{ij}},\\
\hat{F}_{ij} &= -\tfrac{3}{4}\hat{I}_-^{(i)}\hat{I}_-^{(j)}\sin^2\theta_{ij}e^{2i\phi_{ij}},
\end{aligned} \tag{5}$$

where θ_{ij} is the angle between $\mathbf{r}_{ij}$ and the $\hat{z}$ axis, while ϕ_{ij} is the azimuth angle with respect to the $\hat{x}$ axis. The interactions labeled by $\hat{C}_{ij}$, $\hat{D}_{ij}$, $\hat{E}_{ij}$, $\hat{F}_{ij}$ can be neglected under the so-called secular approximation for large magnetic fields. Henceforth, we will neglect these terms in our analytical calculations. In Appendix A we numerically support this consideration. Then, the Hamiltonian (4) reads

$$\hat{H}_n \approx \sum_{i<j}\frac{\beta_{ij}}{4}\big[(\hat{I}_+^{(i)}\hat{I}_-^{(j)} + \hat{I}_-^{(i)}\hat{I}_+^{(j)}) - 4\hat{I}_z^{(i)}\hat{I}_z^{(j)}\big], \tag{6}$$

where $\beta_{ij} = -\frac{\mu_0\gamma_n^2}{4\pi r_{ij}^3}(1 - 3\cos^2\theta_{ij})$.

Considering the zero-field splitting to be larger than the perpendicular magnetic field and the hyperfine coupling, i.e., $D \gg \gamma_e B_x$ and $D \gg \mathcal{A}_{\alpha,\eta}^{(i)}$, one can perform the secular approximation, that neglects $\hat{S}_x$ and $\hat{S}_y$ contributions in the second and third terms in the Hamiltonian (1). We numerically confirm this approximation and consider transverse relaxation in Appendix A. Hence, the Hamiltonian for the tripartite system can be written conditioned to the electron spin manifold, such that

$$\begin{aligned}
\hat{H}_{m_s} = \big(m_s^2 D + m_s\gamma_e B_z\big) + \gamma_n\mathbf{B}\cdot\sum_{i=1}^{N}\mathbf{I}^{(i)}\\
+ m_s\sum_{i=1}^{N}\sum_{\alpha=x,y,z}\mathcal{A}_{z\alpha}^{(i)}\hat{I}_\alpha^{(i)} \quad + \hat{H}_n.
\end{aligned} \tag{7}$$

III. DYNAMICAL QUANTUM PHASE TRANSITION

Nonequilibrium phase transitions give rise to different dynamics that in several cases have no equilibrium counterpart [6,19,39]. The nonequilibrium dynamics originates from different scenarios like Floquet engineering [40–42], reservoir coupling [43,44], quenched parameters [9,14], among others.

In this paper, we focus on dynamical quantum phase transitions (DQPT) driven by a quenched dynamics [9]. For this goal, we consider a Hamiltonian of the form $\hat{H} = \hat{H}_0 + \hat{H}_1$, where $\hat{H}_0$ is the dipolar Hamiltonian in Eq. (6). $\hat{H}_0$ has a $\mathbb{Z}_2$ symmetry that yields a twofold degenerated ground state (all spins up $|\Uparrow\rangle$ or all spins down $|\Downarrow\rangle$). The system is initially prepared in one of the degenerated states, say $|\Psi(0)\rangle = |\Downarrow\rangle$, originating spontaneous symmetry breaking, as witnessed by $\sum_{i=1}^{N}\langle I_z^{(i)}\rangle \neq 0$. Suddenly, $\hat{H}_1$ (to be defined for each example) is turned on and the time evolution is monitored.

It has been shown that the Loschmidt amplitude $\mathcal{G}(t) = \langle\Psi(0)|e^{-i\hat{H}t}|\Psi(0)\rangle$ plays a pivotal role in DQPT [6,9,39,45], resembling the canonical partition function in equilibrium phase transition (EPT). The latter, EPT, is signaled by the nonanalytic behavior of the free energy potential contained in the Lee-Yang zeros of the partition function [46] (also known as Fisher zeros [47]). Thereby, the signature of DQPT shows up when crossing the zeros in the complex time plane, which occurs during the time evolution. The Loschmidt amplitude gives the projection of the time evolved state with the initial state. Additionally, it is also convenient to introduce the Loschmidt echo $P(t) = |\mathcal{G}(t)|^2$, that is interpreted as the return probability to the ground-state manifold. Since this manifold is twofold degenerated, we resorted to use the following extension for the probability: $P(t) = P_{\Downarrow}(t) + P_{\Uparrow}(t)$, with $P_i = |\langle i|e^{-i\hat{H}t}|\Psi(0)\rangle|^2$, and $i = \{\Downarrow, \Uparrow\}$ [6,10,48] (see Appendix B for experimental insights). For simplicity, we restrict our analysis to the case where $P(t)$ exhibits an exponential dependence upon the number of degrees of freedom N. Therefore, we can introduce a rate function as

$$\Lambda(t) = -\lim_{N\to\infty}\frac{1}{N}\log[P(t)]. \tag{8}$$

Then, in analogy with the free energy potential, the nonanaliticity of $\Lambda(t)$ at the critical times t_c probes the DQPT. However, the above expression for $\Lambda(t)$ considers the thermodynamic limit ($N \to \infty$), which can not be always attained in experiments or quantum simulations. Instead, it is worth considering the dominant contribution of the probability, that yields a finite-size signature of DQPT [10,17,49] and our main tool to predict it,

$$\lambda(t) = \min_{\eta\in\{\Downarrow,\Uparrow\}}\left(-\frac{1}{N}\log[P_\eta(t)]\right). \tag{9}$$

We remark that $\lambda(t)$ coincides with $\Lambda(t)$ for large N [6] (see Appendix C). Since the nonanaliticity appears when crossing the region $P_{\Uparrow} = P_{\Downarrow}$, it means that the dynamics restores the symmetry in the ground state probability $P(t)$ initially broken by the state preparation.

Order parameters are crucial to witness quantum phase transitions. In general, one seeks observables that highlight differences between the phases, and exhibit a sudden change when crossing the critical points. Nonequilibrium dynamics demands dynamical order parameters to account for critical times [6,10,50]. Firstly, we will focus on the magnetization as the dynamical order parameter, $\langle M_z\rangle = (1/N)\sum_{i=1}^{N}\langle\hat{I}_z^{(i)}\rangle$, and later on we will discuss the case of quantum correlations, see Appendix D. The former, has signaled DQPT by vanishing when the system restores the symmetry [6].

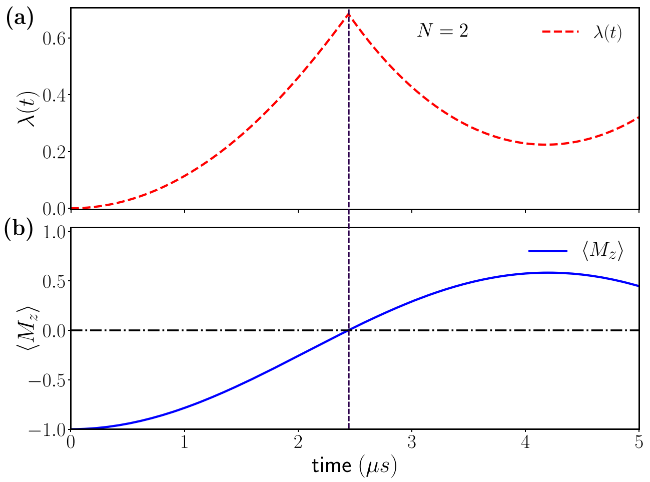

FIG. 2. Nonanalytical points in the rate function $\lambda(t)$ (a) coincides with vanishing magnetization $\langle M_z\rangle$ (b) at critical times. For the simulation we consider two nuclear spins ($N = 2$) and magnetic fields $B_x = 100$ G and $B_z = 50$ G.

A. Quenched dynamics by longitudinal and transverse magnetic fields

First, we focus on the $m_s = 0$ manifold of the NV$^-$ electron spin in Eq. (7). Considering $\theta_{ij} = 0$ we obtain the following Hamiltonian:

$$\begin{aligned}\hat{H} = {}& \frac{\beta_{12}}{2}\left(\left(\hat{I}_+^{(1)}\hat{I}_-^{(2)} + \hat{I}_-^{(1)}\hat{I}_+^{(2)}\right) - 4\hat{I}_z^{(1)}\hat{I}_z^{(2)}\right)\\ &+ \gamma_n B_z\left(\hat{I}_z^{(1)} + \hat{I}_z^{(2)}\right) + \gamma_n B_x\left(\hat{I}_x^{(1)} + \hat{I}_x^{(2)}\right),\end{aligned} \tag{10}$$

where $\hat{I}_\pm^{(i)} = \hat{I}_x^{(i)} \pm i\hat{I}_y^{(i)}$ and hereafter we set $\beta_{12}/2\pi = 4$ kHz. We identify $\hat{H}_0$ and $\hat{H}_1$ with the first and second line in Eq. (10), respectively. Hence, in the absence of magnetic field, the dynamics is governed by $\hat{H}_0$, which has a twofold degenerated ground state, given by $|\downarrow\downarrow\rangle = |\Downarrow\rangle$ and $|\uparrow\uparrow\rangle = |\Uparrow\rangle$.

In Fig. 2(a) we show that ^{13}C nuclear spins surrounding the NV$^-$ center undergo a DQPT. The DQPT is witnessed through nonanalyticities in the rate function $\lambda(t)$ at the critical time $t_{c_1} = 2.4$ μs. Furthermore, in Fig. 2(b) we show the evolution of the magnetization (dynamical order parameter) that, as mentioned above, vanishes at the critical time t_{c_1}. For completeness, we show in Appendix C that the critical time holds when increasing the number of nuclear spins.

In last years, the transverse Ising model has been a playground for the study of dynamical quantum phase transitions [9,10,15]. However, color centers in diamond offer an ubiquitous solid-state platform for extending this model. The central spin given by the electron spin of the NV$^-$ serves as a control qubit upon the nuclear spins [32,51]. Moreover, dipolar coupling between nuclear spins raises a complex dynamics that can be further controlled with a bias off-axis magnetic field. We numerically show here that the relation between the transverse (B_z) and longitudinal (B_x) magnetic fields define the region where DQPT takes place, as shown in Fig. 3(a). The bottom region, where the DQPT fails, is characterized by a negative value in the averaged magnetization. For illustration, in Figs. 3(b) and 3(c), we show the magnetization as a function of B_x and time for fixed amplitudes of B_z. When moving

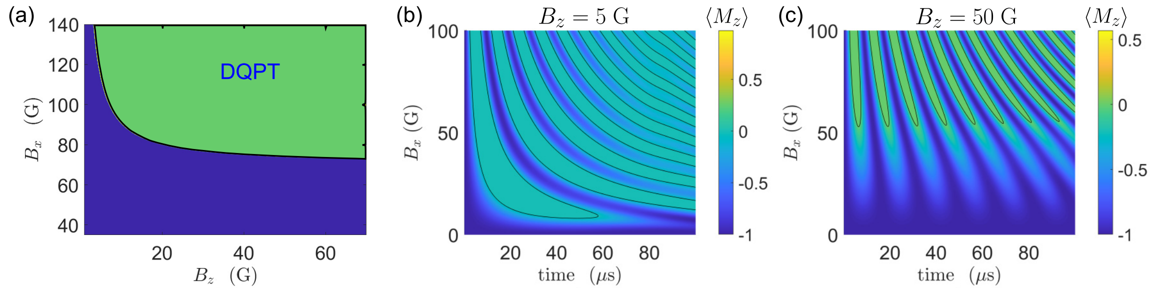

FIG. 3. Phase diagrams for the dynamical quantum phase transition. In panel (a) we vary magnetic fields B_x and B_z to find the regions where dynamical quantum phase transition exists (does not exist), which is illustrated by the green (blue) colored area. The magnetization as a function of time and the magnetic field B_x is calculated for $B_z = 5$ G (b) and $B_z = 50$ G (c). The solid-black lines show the regions where $\langle M_z\rangle = 0$.

ahead in time, one can observe multiples DQPT signaled by the zero-magnetization threshold. Nevertheless, by increasing the transverse field up to $B_z = 50$ G, we observe that there is a broader region for the longitudinal field where no DQPT appears [Fig. 3(c)].

B. Quenched dynamics by a central spin

A depart from quenched parameters can be worked out with a sudden change of the electron spin manifold. This provides a route towards studying DQPT. The NV$^-$ acting as a central spin conditions the ^{13}C nuclear spins Hamiltonian, beyond previously studied models. In contrast to the previous section, here the transverse and longitudinal magnetic fields are replaced by the isotropic and anisotropic hyperfine couplings. For practical reasons, we do consider a small bias magnetic field $B_z = 17$ G. This field lifts the degeneracy in the $m_s = \pm 1$ states and allows us to selectively address state $m_s = +1$. A nucleus-independent rotation (hard π pulse) on the electron spin can be achieved with a Rabi frequency $\sim$8 MHz [52], which approximates the rotation to be instantaneous, as compared with the dipolar interaction $\hat{H}_0$ [first line in Eq. (10)]. We begin by preparing the system in one of the $\hat{H}_0$ eigenstates (for $B_z = 0$), $|0 \downarrow\downarrow\rangle$. Then, after turning on B_z, the quenched dynamics originates from the instantaneous rotation of the electron spin to state $|+1\rangle$, that transforms the Hamiltonian to $\hat{H} = \hat{H}_0 + \hat{H}_1$, with $\hat{H}_1$ given by

$$\begin{aligned}\hat{H}_1 = {} & D\hat{S}_z^2 + \hat{S}_z\mathcal{A}_{zz}^{(1)}\hat{I}_z^{(1)} + \hat{S}_z\mathcal{A}_{zz}^{(2)}\hat{I}_z^{(2)} \\ & + \tfrac{1}{2}\hat{S}_z\mathcal{A}_{\text{ani}}^{(1)}\big(\hat{I}_+^{(1)}e^{-i\phi_1} + \hat{I}_-^{(1)}e^{i\phi_1}\big) \\ & + \tfrac{1}{2}\hat{S}_z\mathcal{A}_{\text{ani}}^{(2)}\big(\hat{I}_+^{(2)}e^{-i\phi_2} + \hat{I}_-^{(2)}e^{i\phi_2}\big),\end{aligned} \tag{11}$$

where $\mathcal{A}_{\text{ani}}^{(i)} = (\mathcal{A}_{zx}^{(i)2} + \mathcal{A}_{zy}^{(i)2})^{1/2}$ and $\tan\phi_i = \mathcal{A}_{zy}^{(i)}/\mathcal{A}_{zx}^{(i)}$. Note that we have omitted the electron and nuclear Zeeman interactions from the bias magnetic field because they have no effect on the DQPT. But we do consider it in our numerical calculations. Next, we study DQPT as the probability to return to the initial state in the nuclear spins manifold ($|\downarrow\downarrow\rangle$) after the time evolution under the total Hamiltonian $\hat{H}$ for the electron spin manifold $m_s = +1$. In Fig. 4 we show the rate function $\lambda(t)$ and the magnetization $\langle M_z\rangle$ for the following set of ^{13}C nuclear spins, $\mathcal{A}_{zz}^{(1)} = -27$ kHz, $\mathcal{A}_{zz}^{(2)} = -28$ kHz, $\mathcal{A}_{\text{ani}}^{(1)} = 128$ kHz, and $\mathcal{A}_{\text{ani}}^{(2)} = 19$ kHz [53].

Our simulations reveal a DQPT for the novel quenching we are considering here. It is important to notice that the DQPT appears when the anisotropic hyperfine coupling ($\mathcal{A}_{\text{ani}}^{(i)}$) is greater than the isotropic one ($\mathcal{A}_{zz}^{(i)}$). We support this statement with numerical simulations with the parameters sets reported in Refs. [53,54]. In contrast, the rate function does not present nonanalytical points and the magnetization always remains negative when the anisotropic component is weaker than the isotropic one, as observed for $\mathcal{A}_{zz}^{(1)} = 2.281$ MHz, $\mathcal{A}_{zz}^{(2)} = 1.884$ MHz, $\mathcal{A}_{\text{ani}}^{(1)} = 0.240$ MHz, and $\mathcal{A}_{\text{ani}}^{(2)} = 0.208$ MHz [55].

In summary, we have considered two different quenched dynamics driven by: (i) external magnetic fields, and (ii) a central electron spin. Starting from a dipolar Hamiltonian [Eq. (6)] with $\mathbb{Z}_2$ symmetry, a spontaneous symmetry breaking appears after the preparation of the initial state. Furthermore, each of the above quenching explicitly breaks this symmetry. Nevertheless, we found that the time evolution tries to restore the original symmetry by matching the ground-state probabilities $P_\Downarrow = P_\Uparrow$, signaling a DQPT.

IV. DYNAMICAL STEERING VIA TIME-VARYING MAGNETIC FIELD

For concreteness, hereafter we focus on the quenched dynamics triggered by the magnetic fields. The competition

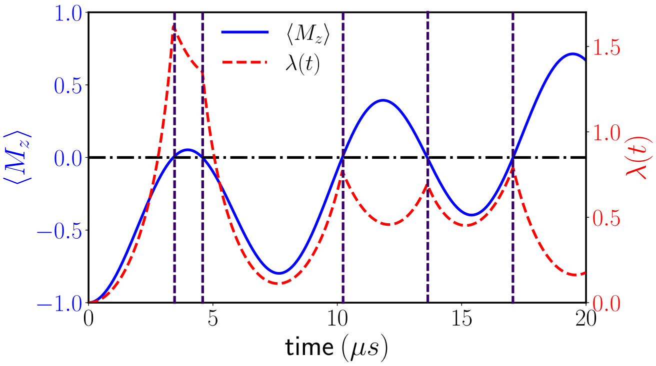

FIG. 4. The quenched dynamics induced by the central spin (NV$^-$) leads to DQPT, as witnessed by the rate function (dashed-red line) and magnetization (solid-blue line). The dotted vertical lines correspond to the times where the rate function is nonanalytical and coincides with a vanishing magnetization.

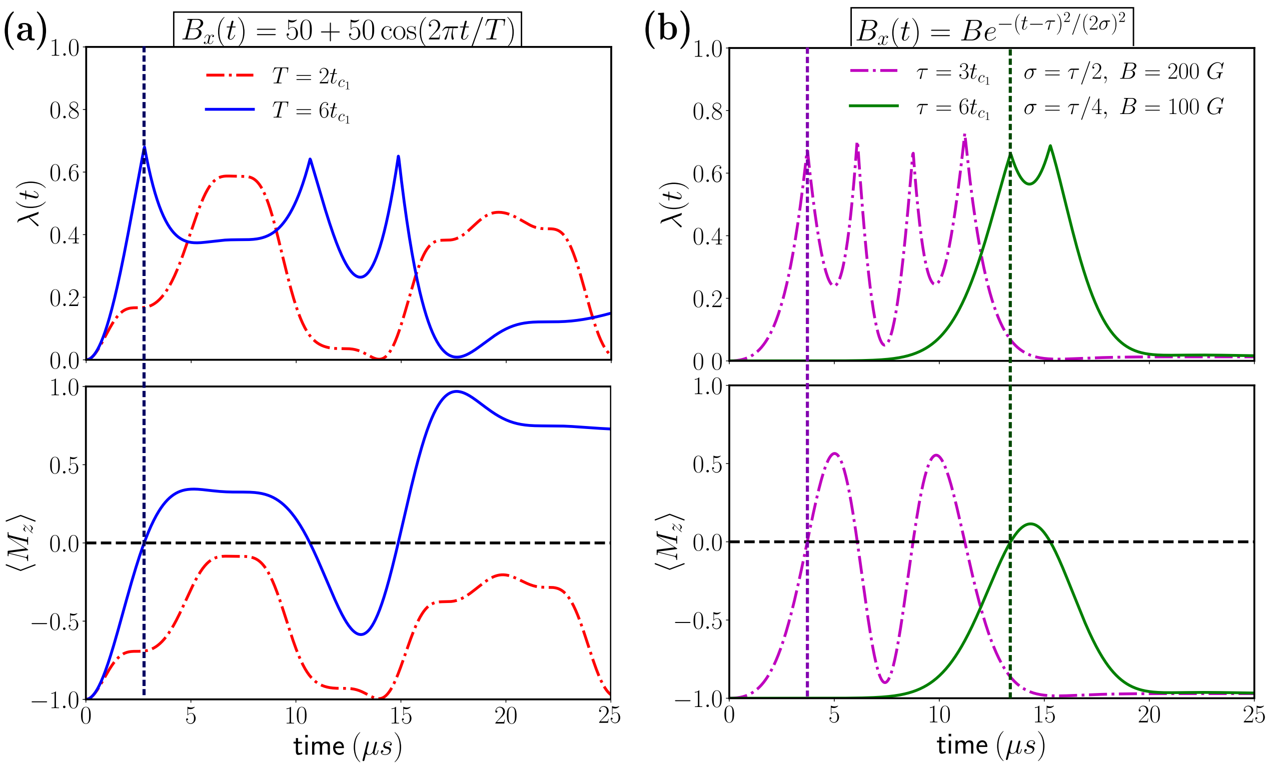

FIG. 5. Controlling dynamical quantum phase transition via time-varying magnetic fields. In the top (bottom) panels we show the rate function $\lambda(t)$ (magnetization $\langle M_z \rangle$). (a) With an oscillatory field $B_x(t)$ we are able to steer the DQPT by controlling the period. Here, we reach a maximum field $B_x(t)$ that amounts to 100 G. t_{c_1} is the critical time for the rate function when the magnetic field is fixed to $B_x = 100$ G, see Fig. 2. (b) With a Gaussian field we have more control on the DQPT, where we can change the critical time and the number of critical points. For all the simulations we considered a closed dynamics under the secular approximation with the initial state $|\downarrow\downarrow\rangle$ for $m_s = 0$, and $B_z = 50$ G.

between the longitudinal and transverse magnetic fields allows us to dynamically steer the DQPT. Let us begin by considering the Hamiltonian $\hat{H}$ in Eq. (10) with a time-dependent magnetic field $B_x(t)$, and we calculate the probabilities according to this time-dependent Hamiltonian.

In what follows, we study the effect of two different fields,

$$B_x(t) = B_{x0} + A\cos\left(\frac{2\pi t}{T}\right), \quad \text{oscillating field,} \quad (12)$$

$$B_x(t) = Be^{-(t-\tau)^2/(2\sigma^2)}, \quad \text{Gaussian field.} \quad (13)$$

First, the oscillating field represents a sinusoidal signal that oscillates around the value $B_{x0} = 50$ G with period T and amplitude $A = 50$ G. Second, the Gaussian field describes a localized pulse around the time τ with a characteristic width σ and amplitude B. In Fig. 5 we show the behavior of the rate function $\lambda(t)$ (top panel) and the magnetization $\langle M_z \rangle$ (bottom panel). From the oscillating field, Fig. 5(a), we note that depending on the period the system may undergo a DQPT. To understand this, we remark that our setting for the fields is similar to the one in Fig. 2, where the first DQPT takes place at the critical time $t_{c_1} \approx 2.4\ \mu$s for a constant field $B_x = 100$ G. Considering the oscillating field for $T = 2t_{c_1}$, we realize that the accumulated action of the field $\int_0^{t_{c_1}} dt\, B_x(t)$ is smaller than that for the constant field in Fig. 2, and hence there is no DQPT. For the case $T = 6t_{c_1}$, the action of the field occurs for a longer time, which yields a DQPT. The main conclusion here is that the accumulated action of the magnetic field can be used to control whether the DQPT occurs by sweeping this quantity near a threshold region.

The above result enables us to define the control in terms of an effective area. Therefore, the Gaussian field is more suitable since it steers the DQPT, allowing us to set the time where the DQPT occurs, and also the number picks (crossings) in λ ($\langle M_z \rangle$), see Fig. 5(b). To summarize, we can steer the DQPT in a nonequilibrium dynamics by controlling a time-dependent magnetic field.

A. Applications in quantum metrology

Spin-spin interaction is a central topic in quantum physics, and the precise knowledge of the strength of this interaction is a key aspect. There are several approaches for estimating the coupling strength, each one with pros and cons depending on the system, noises, measurement apparatus, etc. In particular, the estimation of the coupling strength between two ^{13}C nuclear spins in diamond has attracted attention. For instance, in the seminal work in Ref. [56], the authors considered a simple sequence comprising the initialization of the tripartite system (NV$^-$ and two ^{13}C), followed by time evolution and subsequent measurement on one of the nuclear spins. A more elaborated scheme based on weak measurement has been proposed to estimate the hyperfine coupling between the NV$^-$ and a ^{13}C [57], which could be also extended to

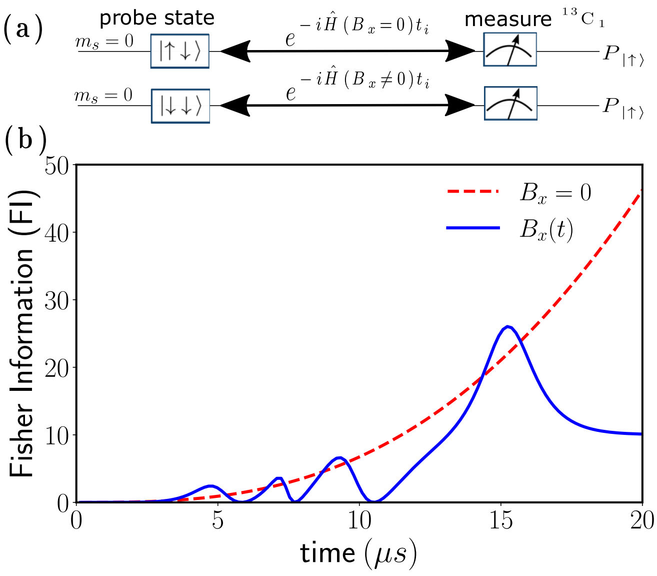

FIG. 6. (a) Two different measurement strategies for the Fisher information, the second involves DQPT. (b) DQPT driven by a Gaussian longitudinal magnetic field improves the Fisher Information corresponding to the dipolar coupling β_{12}, as compared to the case without DQPT at $B_x = 0$. We used $B_x(t) = B\exp\{-(t-\tau)^2/(2\sigma^2)\}$, with $B = 200$ G, $\tau = 3t_{c_1}$, and $\sigma = \tau/2$. $B_z = 50$ G is fixed for both cases.

determine the interaction between two ^{13}C. In this paper, we provide an alternative viewpoint for this task, which involves a proof-of-principle demonstration of the role of nonequilibrium dynamics for quantum metrology. Previous papers dealing with parameter estimation around critical points have focused on the Ising model and delivered opposite outcomes for slightly different purposes [11,12]. Here, we contribute to the ongoing debate by showing that DQPT provides an advantage for quantum metrology.

In what follows, we use the Fisher information (FI) to quantify the amount of information that can be retrieved from the dipolar coupling strength (β_{12}) between the two ^{13}C for a particular measurement scheme. FI of an unknown parameter x is defined as

$$\mathrm{FI}(x) = \sum_i \frac{1}{P_i(x)}\left(\frac{dP_i(x)}{dx}\right)^2, \tag{14}$$

where $P_i(x)$ is the probability of the measurement outcome i and the sum is over all the outcomes. Our measurement strategy involves measurements on one of the nuclear spins, which provides two possible outcomes, the probability of being in spin up ($P_{|\uparrow\rangle}(\beta_{12})$) or spin down [$P_{|\downarrow\rangle}(\beta_{12}) = 1 - P_{|\uparrow\rangle}(\beta_{12})$]. Hence, the FI reduces to

$$\mathrm{FI}(\beta_{12}) = \frac{1}{P_{|\uparrow\rangle}(\beta_{12})(1 - P_{|\uparrow\rangle}(\beta_{12}))}\left[\frac{dP_{|\uparrow\rangle}(\beta_{12})}{d\beta_{12}}\right]^2. \tag{15}$$

The measurement strategy considers the initialization of the system in a probe state, the time evolution under the Hamiltonian $\hat{H}$ in Eq. (10) for a certain interrogation time (t_i), followed by a measurement on the nuclear spin [see Fig. 6(a)]. We analyze two particular cases for the longitudinal component of the magnetic field and probe state (i) $B_x = 0$ with $|\psi(0)\rangle = |\uparrow\downarrow\rangle$; and (ii) $B_x(t) = Be^{-(t-\tau)^2/(2\sigma^2)}$ with $|\psi(0)\rangle = |\downarrow\downarrow\rangle$. The transverse component remains constant for both cases ($B_z = 50$ G) and the electron spin is fixed in $m_s = 0$.

In Fig. 6(b) we show the evolution of the FI. We observe that in the absence of a longitudinal magnetic field $B_x = 0$ (resembling the protocol in Ref. [56]), the FI follows a quadratic evolution, $\mathrm{FI} = t^2$. Details of the calculation are given in Appendix E. In the presence of the Gaussian field [in the DQPT regime shown in Fig. 5(b)], the FI shows oscillations that outperform the previous result. We remark that the time-varying field is crucial for this enhancement since a constant magnetic field B_x delivers no improvement. Hence, we demonstrate that improved metrology can be attained in color centers in diamond by driving the system around critical points.

B. Quantum correlations in stationary magnetization

Another important case of nonequilibrium dynamics appears when studying the steady state of the system in terms of the order parameter, e.g., the asymptotic behavior of the magnetization. For instance, this problem has been addressed in the transverse Ising model with long range interactions [16,49,58], where it was found a connection between DQPT and this nonequilibrium criticality (that is another kind of DQPT). In this section we show that even when the magnetization reaches a steady state, quantum correlations (nondiagonal elements of the density matrix) oscillate between the maximum and minimum values of concurrence [59]. We begin with the system prepared in state $|\downarrow\downarrow\rangle$ ($m_s = 0$) and perform a quench over the magnetic fields from zero to: $B_z = 50$ G and B_x as given in Fig. 7.

In Fig. 7(a) we show the time evolution of the magnetization and the rate function, that rapidly reach a stationary state. In Fig. 7(b) we show that the concurrence [$\mathcal{C}(t)$] follows a periodic behavior in the longtime evolution, see the inset. From Fig. 7(b) we retrieved the disentangled and the maximally entangled states to be of the form

$$|\psi\rangle = r(e^{i\varphi_1}|\uparrow\uparrow\rangle + e^{i\varphi_2}(|\uparrow\downarrow\rangle + |\downarrow\uparrow\rangle) + e^{i\varphi_3}|\downarrow\downarrow\rangle), \tag{16}$$

with $r \approx 1/2$. On the one hand, the maximally entangled state ($\mathcal{C} \approx 1$ [59]) is given by $\{\varphi_1 = 0.31, \varphi_2 = 1.16, \varphi_3 = -1.13\}$. On the other hand, the disentangled state ($\mathcal{C} \approx 0$) is $\{\varphi_1 = -0.59, \varphi_2 = 0.11, \varphi_3 = 0.82\}$. The definition and other calculations with the concurrence ($\mathcal{C}$) are given in Appendix D.

We remark that entanglement (or quantum correlation in general) ranks among the most distinguishing features in quantum mechanics. Therefore, it is worth studying its connection with DQPT [10], critical points [60], or spontaneous symmetry breaking [61]. In our simulations we show that DQPT can be accompanied by to different behaviors of entanglement. On the one hand, in Appendix D we show that the rate function exhibits a periodic behavior while the concurrence follows a longtime monotonic behavior—see Figs. 11 and 12. On the other hand, we show in Fig. 7 that one can steer the rate function to reach a stationary value, driving the entanglement to an oscillatory behavior. A detailed analysis of this connection it is left for a future work.

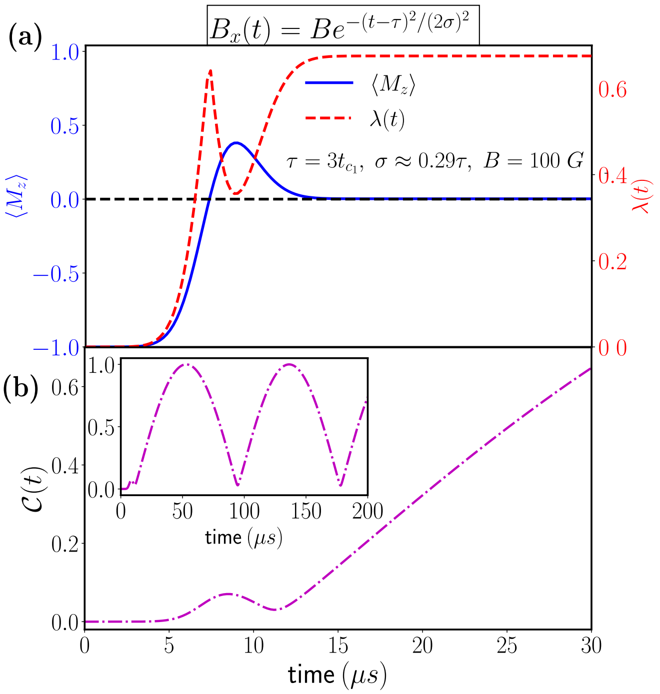

FIG. 7. (a) Evolution of the rate function $\lambda(t)$ (dashed-red line) and magnetization (solid-blue line) for a Gaussian field. The magnetization reaches a steady state that is adjusted around $\langle M_z \rangle = 0$. (b) The concurrence shows oscillations even when the magnetization has been frozen, and amounts to one, indicating the creation of a maximally entangled state.

V. CONCLUSIONS

In this paper we proposed a negatively charged nitrogen-vacancy (NV$^-$) center and nearby carbon-13 (^{13}C) nuclear spins as a testbed for studying dynamical quantum phase transition (DQPT). We found two different quenched dynamics that enforce DQPT on the nuclear spins. First, we observed that nuclear spins undergo DQPT by appropriately choosing the relation between the transverse and longitudinal components of an external magnetic field. Moreover, one can steer the DQPT via a time-dependent longitudinal magnetic field. In addition, this dynamical steering can be harnessed to enhance the Fisher Information concerning the estimation of the coupling strength between two ^{13}C nuclear spins. Second, by rapidly rotating the NV$^-$ electron spin (that is a central spin), the ^{13}C nuclear spins undergo a DQPT depending on the relation between the anisotropic and isotropic coupling of the hyperfine interaction. We also studied the role of bipartite and tripartite entanglement during the critical points where DQPT takes place, and in the steady state of the magnetization. Overall, we believe that NV$^-$ and surrounding nuclear spins provide a prototype for studying nonequilibrium dynamics, and in particular, DQPT.

ACKNOWLEDGMENTS

We thank M. Chen and A. Mendoza-Coto for fruitful discussions. F.J.G. acknowledges support from Universidad Mayor through the Doctoral Fellowship. A.N. acknowledges financial support from Universidad Mayor through the Postdoctoral Fellowship. R.C. acknowledges support from Fondecyt Iniciación No. 11180143.

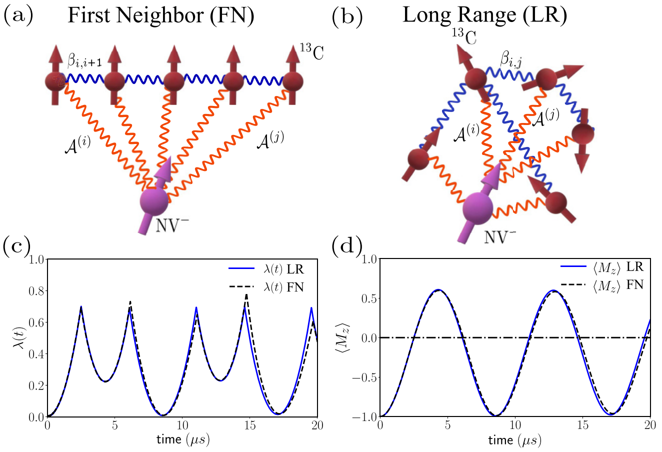

FIG. 8. A randomly generated sample with long range interactions exhibits a similar signature of finite-size DQPT as compared to the simplified linear model with fixed orientations and first-neighbor interaction. We have varied the hyperfine interaction and dipolar coupling in the range of few kHz.

APPENDIX A: SECULAR APPROXIMATION AND RELAXATION

Throughout this paper, we considered a lossless scenario and the secular approximation. The latter allows us to simplify the analytical calculations by restricting the Hamiltonian to be conditioned to the NV$^-$ electron spin manifold. This approximation breaks down when $D \lesssim \gamma_e B_x$, and hence the Zeeman terms $\hat{S}_x$ and $\hat{S}_y$ must be considered. Furthermore, we shall consider magnetic noise on the NV$^-$ and ^{13}C nuclear spins. When the electron spin is in the $m_s = 0$ manifold, we considered it isolated from magnetic noise. However, when the electron spin occupies states $m_s = \pm 1$ (which occurs without the secular approximation) a transverse relaxation process must be taken into account [28,32]. The NV$^-$ electron spin coherence time typically ranges from 4 to 10 μs [25]. We resorted to use $T_2^\star = 7\ \mu$s, which provides enough time to observe the DQPT in Fig. 4. To support our results given in the main text, we include the full Hamiltonian (without secular approximation) and including transverse relaxation over the electron and nuclear spins with a coherence time $T_{2n}^\star = 0.5$ ms [32]. We find that for magnetic fields below $B_x = 500$ G, our simplified model reproduce very well the magnetization up to 70 μs. The rate function $\lambda(t)$, which is less important for the physical validation of the model, behaves well up to 20 μs. The reason behind this is the logarithmic function in its definition that increases the mismatch.

In addition, we generalized our linear model to the case where the nuclear spins are randomly placed in the diamond sample with random orientations. We vary the hyperfine couplings $\mathcal{A}^{(i)}$ from few to few tens of kHz, the dipolar interaction $\beta_{ij} = \mu_0 \gamma_n^2 / 4\pi r_{ij}^3$ ranges from zero to 4 kHz, and $\theta_{ij} \in [0, \pi]$ and $\phi_{ij} \in [0, \pi/2]$ [see Eq. (5)]. These calculations also include noise and all nonsecular terms. In Fig. 8 we show that

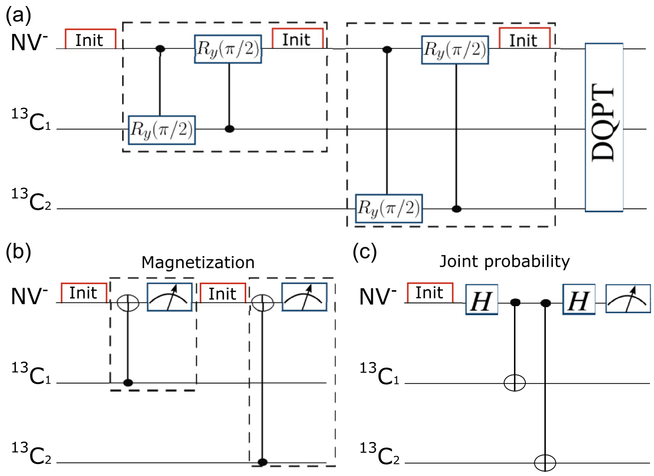

FIG. 9. Wired diagram for the initialization and read out processes. (a) The "Init" box stands for the $\lambda = 637$ nm laser that resets the NV$^-$. Each dashed box encapsulates the initialization sequence for a ^{13}C nuclear spin. The "DQPT" box stands for the main sequence to obtain the dynamical quantum phase transition, either the variation of the fields or the electron spin rotation. (b) Each dashed box measures the corresponding $\langle I_z^{(i)} \rangle$ expectation value for the calculation of the averaged magnetization. (c) The sequence performs a partial two-qubit tomography $\langle I_z^{(1)} I_z^{(2)} \rangle$ to determine $P_\Uparrow(t)$ and $P_\Downarrow(t)$.

for the firsts cusp (nonanalyctic points) in $\lambda(t)$ there is no significant difference between these models, and the DQPT holds. We perform several realizations and observe similar behaviors.

APPENDIX B: INITIALIZATION AND READ OUT

In this section we briefly describe the initialization and read out processes to obtain the probabilities $P_\Uparrow(t) = |0 \uparrow\uparrow\rangle$ and $P_\Downarrow(t) = |0 \downarrow\downarrow\rangle$ [for the calculation of the rate function $\lambda(t)$ in Eq. (10)] and the averaged magnetization $\langle M_z \rangle = (1/2)\sum_{i=1}^{2} \langle \hat{I}_z^{(i)} \rangle$. For simplicity, we focus on the cryogenic temperature regime, ~4 K, where single-shot read out of the electron spin can be performed with high fidelity. Initialization of the electron spin in $m_s = 0$ manifold is achieved with a resonant 637 nm laser by optical pumping. The ^{13}C nuclear spins are sequentially initialized through a polarization transfer gate that maps the polarized electron spin onto the nuclear spin, and a reset of the electron spin [31,33,34].

Optical read out of the NV$^-$ electron spin is driven by the resonant 637 nm red laser via spin-dependent fluorescence. Individual read out of ^{13}C nuclear spins can be achieved by first mapping its state onto the electron spin and subsequently read out the electron spin [33,56,62]. We propose this sequence to measure each expectation value $\langle \hat{I}_z^{(i)} \rangle$ that contributes to the averaged magnetization. For the estimation of the joint probability $P_\Uparrow(t)$ and $P_\Downarrow(t)$ we resorted to propose a two-qubit state tomography, where we are only interested in the parallel contribution $\langle I_z^1 I_z^2 \rangle$. The initialization and read out processes are pictured in Fig. 9.

We note that we provided a proof-of-principle demonstration of a single conduction of the experiment. Further elaboration on the experimental process may consider optimal approach depending on the strength of the hyperfine coupling [63], or simultaneous initialization and read out [64,65]. Moreover, in the case of room temperature one may consider an ancilla qubit for single-shot read out [66], or Bayesian estimation [67] instead.

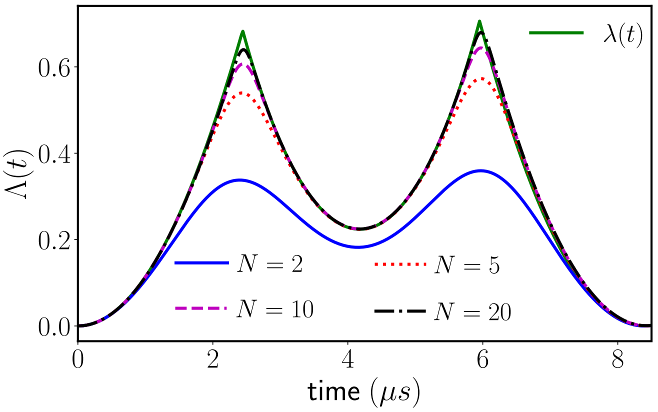

FIG. 10. Evolution of the rate function for different numbers of spins. The universality of the critical time holds. $\lambda(t)$ has the same behavior independent of the number of spins.

APPENDIX C: SCALABILITY

Throughout this paper we have focused on the finite-size signatures of DQPT as witnessed by the rate function $\lambda(t)$ in Eq. (9). This function should agree with the more general rate $\Lambda(t)$ defined in Eq. (8) for large N, given that in this regime the probability is dominated by one of the two contributions $P_\Uparrow$ or $P_\Downarrow$ [10]. We numerically find that for our particular problem $\lambda(t)$ rapidly converges to a universal critical time t_c for the DQPT, with no finite-size corrections observed as the number of spins N increases (we performed simulations up to $N = 20$ spins). To illustrate further that this behavior predicts the thermodynamic limit, we focus on the scaling of the rate function $\Lambda(t)$. $\Lambda(t)$ shows a smooth behavior at t_c, but it becomes sharper when increasing N and rapidly approaches $\lambda(t)$. The results are shown in Fig. 10. For the calculations, we consider a fixed geometry of a 1D array of nuclear spins with the same coupling strength given by

$$\hat{H} = \gamma_e B_z \sum_{i=1}^{N} \hat{I}_z^{(i)} + \gamma_n B_x \sum_{i=1}^{N} \hat{I}_x^{(i)} + \sum_{i=1}^{N-1} \frac{\beta}{2}\left(\left(\hat{I}_+^{(i)} \hat{I}_-^{(i+1)} + \hat{I}_-^{(i)} \hat{I}_+^{(i+1)}\right) - 4\hat{I}_z^{(i)} \hat{I}_z^{(i+1)}\right), \quad \text{(C1)}$$

with $\beta/2\pi = 4$ kHz, $B_x = 100$ G, and $B_z = 50$ G.

APPENDIX D: ENTANGLEMENT AS ORDER PARAMETER

In the past, it has been shown that critical points corresponding to DQPT yield increased quantum correlations [10]. Here, we contribute to this analysis by showing the same behavior for the entanglement, but also by shedding light on the multipartite entanglement. First, we quantify the

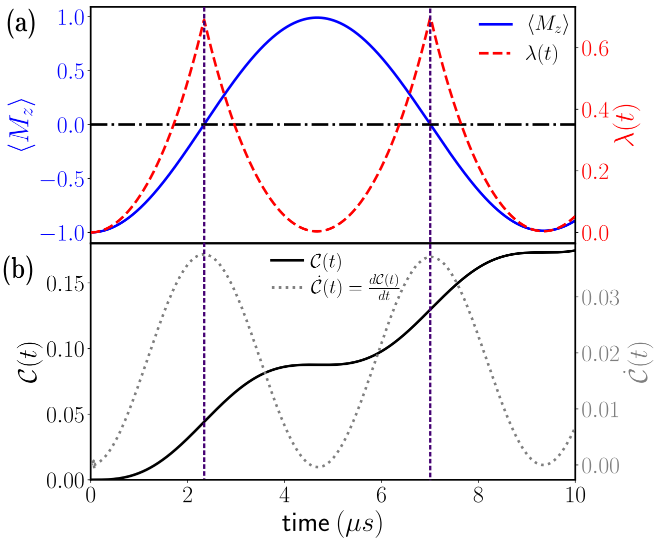

FIG. 11. Concurrence increases in the regions where the rate function $\lambda(t)$ becomes nonanalytic, signaling a maximum in its derivative. $B_x = 100$ G and $B_z = 5$ G.

entanglement by the concurrence [59], that is defined as

$$\mathcal{C}(\rho_{12}) = \max(\lambda_1 - \lambda_2 - \lambda_3 - \lambda_4, 0), \qquad \text{(D1)}$$

where the λ_i are the square roots of the eigenvalues, in decreasing order, of the matrix $\mathbf{R} = \hat{\rho}_{12}(\hat{I}_y^{(1)} \otimes \hat{I}_y^{(2)})\hat{\rho}_{12}^*(\hat{I}_y^{(1)} \otimes \hat{I}_y^{(2)})$. $\hat{\rho}_{12}^*$ is the complex conjugate of the density operator of the bipartite system corresponding to the two ^{13}C nuclear spins.

In Fig. 11 the concurrence evidences the generation of quantum correlations between the two spins when the rate function presents nonanalytical points, in agreement with Ref. [10]. Furthermore, its derivative $[\dot{\mathcal{C}}(t)]$ is maximum at these points. For this plot we followed the dynamics discussed in Sec. III A.

Second, we pay attention to the generation of multipartite entanglement. To this end, we consider three nuclear spins. Then, the Hamiltonian for this new system, conditioned to the NV$^-$ electron spin in the $m_s = 0$ manifold reads

$$\begin{aligned}\hat{H} &= \gamma_e B_z \sum_{i=1}^{3} \hat{I}_z^{(i)} + \gamma_n B_x \sum_{i=1}^{3} \hat{I}_x^{(i)} \\ &\quad + \frac{\beta_{12}}{2}\big(\big(\hat{I}_+^{(1)}\hat{I}_-^{(2)} + \hat{I}_-^{(1)}\hat{I}_+^{(2)}\big) - 4\hat{I}_z^{(1)}\hat{I}_z^{(2)}\big) \\ &\quad + \frac{\beta_{23}}{2}\big(\big(\hat{I}_+^{(2)}\hat{I}_-^{(3)} + \hat{I}_-^{(2)}\hat{I}_+^{(3)}\big) - 4\hat{I}_z^{(2)}\hat{I}_z^{(3)}\big). \qquad \text{(D2)}\end{aligned}$$

For simplicity, we consider the spins in a 1D-array configuration with first-neighbors interaction and $\beta_{12} = \beta_{23} = \beta$. Throughout this paper we have set $\beta/2\pi = 4$ kHz. To quantify multipartite entanglement we use the tangle (τ) [68],

$$\tau_{123} = \mathcal{C}_{1(23)}^2 - \mathcal{C}_{12}^2 - \mathcal{C}_{13}^2, \qquad \text{(D3)}$$

where τ_{123} represents a residual entanglement of the collective three spins system [68], and $\mathcal{C}_{1(23)}^2 = 2(1 - \mathrm{Tr}[\rho_1^2])$ represents the entanglement between ^{13}C$_1$ and pair ^{13}C$_2 - {}^{13}$C$_3$. $\mathcal{C}_{12}$ and $\mathcal{C}_{13}$ stand for the concurrence of the bipartite systems given by Eq. (D1).

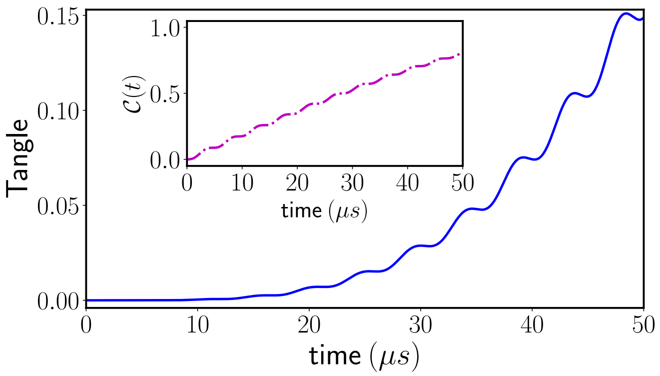

FIG. 12. Multipartite entanglement increases during the time evolution. After several critical points the plateaus show up, indicating a similar behavior with the concurrence in Fig. 11. Inset: Longtime behavior of the concurrence. $B_x = 100$ G and $B_z = 5$ G.

Figure 12 shows the evolution of the tangle (τ_{123}) for the tripartite system made up of three ^{13}C nuclear spins. We note that at early evolution, the tangle is approximately zero since it takes time for bipartite entanglement to built up first. After ~15 μs, the tangle increases, and the plateaus appear, coinciding with the minimum of the rate function $\lambda(t)$ (similar to the concurrence in Fig. 11). For comparison, in the inset we show the longtime behavior of the concurrence.

APPENDIX E: FISHER INFORMATION CORRESPONDING TO β_{12} FOR $B_x = 0$

To begin with, we consider the Hamiltonian in the $m_s = 0$ manifold given in Eq. (10) for $B_x = 0$,

$$\begin{aligned}\hat{H} &= \gamma_n B_z\big(\hat{I}_z^{(1)} + \hat{I}_z^{(2)}\big) \\ &\quad + \frac{\beta_{12}}{2}\big(\big(\hat{I}_+^{(1)}\hat{I}_-^{(2)} + \hat{I}_-^{(1)}\hat{I}_+^{(2)}\big) - 4\hat{I}_z^{(1)}\hat{I}_z^{(2)}\big). \qquad \text{(E1)}\end{aligned}$$

The corresponding eigenstates and eigenvalues are

$$\begin{aligned}|\psi_1\rangle &= |0\downarrow\downarrow\rangle, \quad E_1 = -\left(\gamma_n B_z + \frac{\beta_{12}}{2}\right), \\ |\psi_2\rangle &= |0\uparrow\uparrow\rangle, \quad E_2 = \gamma_n B_z - \frac{\beta_{12}}{2}, \\ |\psi_3\rangle &= \frac{1}{\sqrt{2}}(|0\downarrow\uparrow\rangle - |0\uparrow\downarrow\rangle), \quad E_3 = 0, \\ |\psi_4\rangle &= \frac{1}{\sqrt{2}}(|0\downarrow\uparrow\rangle + |0\uparrow\downarrow\rangle), \quad E_3 = \beta_{12}. \qquad \text{(E2)}\end{aligned}$$

The initial state (probe state that increases the FI) is $|0\uparrow\downarrow\rangle$, that in the eigenstate basis can be written as

$$|\psi(0)\rangle = |0\uparrow\downarrow\rangle = \frac{1}{\sqrt{2}}(|\psi_4\rangle - |\psi_3\rangle). \qquad \text{(E3)}$$

The evolution of this state reads

$$|\psi(t)\rangle = e^{-i\hat{H}(\beta_{12})t}|\psi(0)\rangle = \frac{1}{\sqrt{2}}\big(e^{-i\beta_{12}t}|\psi_4\rangle - |\psi_3\rangle\big). \qquad \text{(E4)}$$

In the bare basis the density matrix reads (we omitted the electron spin state $|0\rangle$)

$$\begin{aligned}\rho(t) = |\psi(t)\rangle\langle\psi(t)| = \tfrac{1}{4}[&(e^{-i\beta_{12}t}-1)(e^{i\beta_{12}t}-1)|\downarrow\uparrow\rangle\langle\downarrow\uparrow| \\ &+(e^{-i\beta_{12}t}-1)(e^{i\beta_{12}t}+1)|\downarrow\uparrow\rangle\langle\uparrow\downarrow| \\ &+(e^{-i\beta_{12}t}+1)(e^{i\beta_{12}t}-1)|\uparrow\downarrow\rangle\langle\downarrow\uparrow| \\ &+(e^{-i\beta_{12}t}+1)(e^{i\beta_{12}t}+1)|\uparrow\downarrow\rangle\langle\uparrow\downarrow|]. \qquad (E5)\end{aligned}$$

To obtain the reduced density matrix for $^{13}\mathrm{C}_1$ we trace over the $^{13}\mathrm{C}_2$ degrees of freedom,

$$\begin{aligned}\rho_{n_1}(t) &= \mathrm{Tr}_{n_2}[\rho(t)] = \langle\uparrow|_{n_2}\rho(t)|\uparrow\rangle_{n_2} + \langle\downarrow|_{n_2}\rho(t)|\downarrow\rangle_{n_2} \\ &= \sin^2\left(\frac{\beta_{12}t}{2}\right)|\downarrow\rangle\langle\downarrow| + \cos^2\left(\frac{\beta_{12}t}{2}\right)|\uparrow\rangle\langle\uparrow|. \qquad (E6)\end{aligned}$$

Next, we calculate the probability to find the nuclear spin in states $|\uparrow\rangle$ ($P_{|\uparrow\rangle}(\beta_{12})$) and $|\downarrow\rangle(P_{|\downarrow\rangle}(\beta_{12}))$,

$$P_{|\uparrow\rangle}(\beta_{12}) = \cos^2\left(\frac{\beta_{12}t}{2}\right), \qquad (E7)$$

$$P_{|\downarrow\rangle}(\beta_{12}) = 1 - \cos^2\left(\frac{\beta_{12}t}{2}\right) = \sin^2\left(\frac{\beta_{12}t}{2}\right). \qquad (E8)$$

Finally, we replace the above expressions into the Fisher information in Eq. (15) and obtain

$$\mathrm{FI}(\beta_{12}) = t^2. \qquad (E9)$$

---

[1] S. Sachdev, *Quantum Phase Transitions*, 2nd edition (Cambridge University Press, Cambridge, 2011).

[2] K. Toyoda, Y. Matsuno, A. Noguchi, S. Haze, and S. Urabe, Experimental Realization of a Quantum Phase Transition of Polaritonic Excitations, Phys. Rev. Lett. **111**, 160501 (2013).

[3] M. Greiner, O. Mandel, T. Esslinger, T. W. Hänsch, and I. Bloch, Quantum phase transition from a superfluid to a Mott insulator in a gas of ultracold atoms, Nature (London) **415**, 39 (2002).

[4] M.-J. Hwang and M. B. Plenio, Quantum Phase Transition in the Finite Jaynes-Cummings Lattice Systems, Phys. Rev. Lett. **117**, 123602 (2016).

[5] S. Diehl, A. Tomadin, A. Micheli, R. Fazio, and P. Zoller, Dynamical Phase Transitions and Instabilities in Open Atomic Many-Body Systems, Phys. Rev. Lett. **105**, 015702 (2010).

[6] M. Heyl, Dynamical quantum phase transitions: A review, Rep. Prog. Phys. **81**, 054001 (2018).

[7] J. Huber, P. Kirton, and P. Rabl, Nonequilibrium magnetic phases in spin lattices with gain and loss, Phys. Rev. A **102**, 012219 (2020).

[8] D. Tancara, A. Norambuena, R. Peña, G. Romero, F. Torres, and R. Coto, Steering interchange of polariton branches via coherent and incoherent dynamics, Phys. Rev. A **103**, 053708 (2021).

[9] M. Heyl, A. Polkovnikov, and S. Kehrein, Dynamical Quantum Phase Transitions in the Transverse-Field Ising Model, Phys. Rev. Lett. **110**, 135704 (2013).

[10] P. Jurcevic, H. Shen, P. Hauke, C. Maier, T. Brydges, C. Hempel, B. P. Lanyon, M. Heyl, R. Blatt, and C. F. Roos, Direct Observation of Dynamical Quantum Phase Transitions in an Interacting Many-Body System, Phys. Rev. Lett. **119**, 080501 (2017).

[11] C. Invernizzi, M. Korbman, L. Campos Venuti, and M. G. A. Paris, Optimal quantum estimation in spin systems at criticality, Phys. Rev. A **78**, 042106 (2008).

[12] Z. Sun, J. Ma, X.-M. Lu, and X. Wang, Fisher information in a quantum-critical environment, Phys. Rev. A **82**, 022306 (2010).

[13] J. Zhang, G. Pagano, P. Hess, A. Kyprianidis, P. Becker, H. Kaplan, A. V. Gorshkov, Z.-X. Gong, and C. Monroe, Observation of a many-body dynamical phase transition with a 53-qubit quantum simulator, Nature (London) **551**, 601 (2017).

[14] N. Fläschner, D. Vogel, M. Tarnowski, B. S. Rem, D. S. Lühmann, M. Heyl, J. C. Budich, L. Mathey, K. Sengstock, and C. Weitenberg, Observation of dynamical vortices after quenches in a system with topology, Nat. Phys. **14**, 265 (2018).

[15] V. Gurarie, Dynamical quantum phase transitions in the random field Ising model, Phys. Rev. A **100**, 031601(R) (2019).

[16] J. C. Halimeh and V. Zauner-Stauber, Dynamical phase diagram of spin chains with long-range interactions, Phys. Rev. B **96**, 134427 (2017).

[17] M. Heyl, Dynamical Quantum Phase Transitions in Systems with Broken-Symmetry Phases, Phys. Rev. Lett. **113**, 205701 (2014).

[18] R. Jafari, H. Johannesson, A. Langari, and M. A. Martin-Delgado, Quench dynamics and zero-energy modes: The case of the Creutz model, Phys. Rev. B **99**, 054302 (2019).

[19] R. Jafari, Dynamical quantum phase transition and quasi-particle excitation, Sci. Rep. **9**, 2871 (2019).

[20] M. Sadrzadeh, R. Jafari, and A. Langari, Dynamical topological quantum phase transitions at criticality, Phys. Rev. B **103**, 144305 (2021).

[21] M. Atatüre, D. Englund, N. Vamivakas, S. Lee, and J. Wrachtrup, Material platforms for spin-based photonic quantum technologies, Nat. Rev. Mater. **3**, 38 (2018).

[22] D. Awschalom, R. Hanson, J. Wrachtrup, and B. B. Zhou, Quantum technologies with optically interfaced solid-state spins, Nat. Photonics **12**, 516 (2018).

[23] J. Wrachtrup and F. Jelezko, Processing quantum information in diamond, J. Phys.: Condens. Matter **18**, S807 (2006).

[24] B. Hensen, H. Bernien, A. E. Dreau, A. Reiserer, N. Kalb, M. S. Blok, J. Ruitenberg, R. F. L. Vermeulen, R. N. Schouten, C. Abellan, Loophole-free bell inequality violation using electron spins separated by 1.3 kilometres, Nature (London) **526**, 682 (2015).

[25] J. R. Maze, P. L. Stanwix, J. S. Hodges, S. Hong, J. M. Taylor, P. Cappellaro, L. Jiang, M. V. Gurudev Dutt, E. Togan, A. S. Zibrov, A. Yacoby, R. L. Walsworth, and M. D. Lukin, Nanoscale magnetic sensing with an individual electronic spin in diamond, Nature (London) **455**, 644 (2008).

[26] G. Balasubramanian, I. Y. Chan, R. Kolesov, M. Al-Hmoud, J. Tisler, C. Shin, C. Kim, A. Wojcik, P. R. Hemmer, A. Krueger, Nanoscale imaging magnetometry with diamond spins under ambient conditions, Nature (London) **455**, 648 (2008).

[27] C. L. Degen, F. Reinhard, and P. Cappellaro, Quantum sensing, Rev. Mod. Phys. **89**, 035002 (2017).

[28] R. Coto, H. Dinani, A. Norambuena, M. Chen, and J. Maze, Probabilistic magnetometry with two-spin system in diamond, Quantum Sci. Technol. **6**, 035011 (2021).

[29] B. B. Zhou, A. Baksic, H. Ribeiro, C. G. Yale, F. J. Heremans, P. C. Jerger, A. Auer, G. Burkard, A. A. Clerk, and D. D. Awschalom, Accelerated quantum control using superadiabatic dynamics in a solid-state lambda system, Nat. Phys. **13**, 330 (2017).

[30] R. Coto, V. Jacques, G. Hétet, and J. R. Maze, Stimulated raman adiabatic control of a nuclear spin in diamond, Phys. Rev. B **96**, 085420 (2017).

[31] M. H. Abobeih, J. Randall, C. E. Bradley, H. P. Bartling, M. A. Bakker, M. J. Degen, M. Markham, D. J. Twitchen, and T. H. Taminiau, Atomic-scale imaging of a 27-nuclear-spin cluster using a quantum sensor, Nature (London) **576**, 411 (2019).

[32] F. J. González and R. Coto, Decoherence-protected quantum register of nuclear spins in diamond, Quantum Sci. Technol. **7**, 025015 (2022).

[33] G. Waldherr, Y. Wang, S. Zaiser, M. Jamali, T. Schulte-Herbrüggen, H. Abe, T. Ohshima, J. Isoya, J. F. Du, P. Neumann, and J. Wrachtrup, Quantum error correction in a solid-state hybrid spin register, Nature (London) **506**, 204 (2014).

[34] T. H. Taminiau, J. Cramer, T. van der Sar, V. V. Dobrovitski, and R. Hanson, Universal control and error correction in multi-qubit spin registers in diamond, Nat. Nanotechnol. **9**, 171 (2014).

[35] M. W. Doherty, V. M. Acosta, A. Jarmola, M. S. J. Barson, N. B. Manson, D. Budker, and L. C. L. Hollenberg, Temperature shifts of the resonances of the NV$^-$ center in diamond, Phys. Rev. B **90**, 041201(R) (2014).

[36] V. Ivády, T. Simon, J. R. Maze, I. A. Abrikosov, and A. Gali, Pressure and temperature dependence of the zero-field splitting in the ground state of nv centers in diamond: A first-principles study, Phys. Rev. B **90**, 235205 (2014).

[37] F. Jelezko, T. Gaebel, I. Popa, A. Gruber, and J. Wrachtrup, Observation of Coherent Oscillations in a Single Electron Spin, Phys. Rev. Lett. **92**, 076401 (2004).

[38] M. W. Doherty, F. Dolde, H. Fedder, F. Jelezko, J. Wrachtrup, N. B. Manson, and L. C. L. Hollenberg, Theory of the ground-state spin of the NV$^-$ center in diamond, Phys. Rev. B **85**, 205203 (2012).

[39] S. Vajna and B. Dóra, Disentangling dynamical phase transitions from equilibrium phase transitions, Phys. Rev. B **89**, 161105(R) (2014).

[40] V. M. Bastidas, C. Emary, G. Schaller, and T. Brandes, Nonequilibrium quantum phase transitions in the ising model, Phys. Rev. A **86**, 063627 (2012).

[41] K. Yang, L. Zhou, W. Ma Wenchao, X. Kong, P. Wang, X. Qin, X. Rong, Y. Wang, F. Shi, J. Gong, and J. Du, Floquet dynamical quantum phase transitions, Phys. Rev. B **100**, 085308 (2019).

[42] S. Zamani, R. Jafari, and A. Langari, Floquet dynamical quantum phase transition in the extended XY model: Nonadiabatic to adiabatic topological transition, Phys. Rev. B **102**, 144306 (2020).

[43] F. Minganti, A. Biella, N. Bartolo, and C. Ciuti, Spectral theory of Liouvillians for dissipative phase transitions, Phys. Rev. A **98**, 042118 (2018).

[44] T. Fink, A. Schade, S. Höfling, C. Schneider, and A. Imamoglu, Signatures of a dissipative phase transition in photon correlation measurements, Nat. Phys. **14**, 365 (2018).

[45] E. Canovi, P. Werner, and M. Eckstein, First-Order Dynamical Phase Transitions, Phys. Rev. Lett. **113**, 265702 (2014).

[46] C. N. Yang and T. D. Lee, Statistical theory of equations of state and phase transitions. I. Theory of condensation, Phys. Rev. **87**, 404 (1952).

[47] M. E. Fisher, *The Nature of Critical Points* (University of Colorado Press, Boulder, Colorado, 1965).

[48] F. Andraschko and J. Sirker, Dynamical quantum phase transitions and the Loschmidt echo: A transfer matrix approach, Phys. Rev. B **89**, 125120 (2014).

[49] B. Žunkovič, M. Heyl, M. Knap, and A. Silva, Dynamical Quantum Phase Transitions in Spin Chains with Long-Range Interactions: Merging Different Concepts of Nonequilibrium Criticality, Phys. Rev. Lett. **120**, 130601 (2018).

[50] M. Heyl, Quenching a quantum critical state by the order parameter: Dynamical quantum phase transitions and quantum speed limits, Phys. Rev. B **95**, 060504(R) (2017).

[51] A. Cooper, W. K. C. Sun, J.-C. Jaskula, and P. Cappellaro, Identification and Control of Electron-Nuclear Spin Defects in Diamond, Phys. Rev. Lett. **124**, 083602 (2020).

[52] M. S. Blok, C. Bonato, M. L. Markham, D. J. Twitchen, V. V. Dobrovitski, and R. Hanson, Manipulating a qubit through the backaction of sequential partial measurements and real-time feedback, Nat. Phys. **10**, 189 (2014).

[53] A. Dréau, P. Jamonneau, O. Gazzano, S. Kosen, J.-F. Roch, J. R. Maze, and V. Jacques, Probing the Dynamics of a Nuclear Spin Bath in Diamond through Time-Resolved Central Spin Magnetometry, Phys. Rev. Lett. **113**, 137601 (2014).

[54] A. Reiserer, N. Kalb, M. S. Blok, K. J. M. van Bemmelen, T. H. Taminiau, R. Hanson, D. J. Twitchen, and M. Markham, Robust Quantum-Network Memory Using Decoherence-Protected Subspaces of Nuclear Spins, Phys. Rev. X **6**, 021040 (2016).

[55] A. P. Nizovtsev, S. Ya Kilin, A. L. Pushkarchuk, V. A. Pushkarchuk, and F. Jelezko, Theoretical study of hyperfine interactions and optically detected magnetic resonance spectra by simulation of the $\mathrm{C}_{291}[NV]_{-H172}$ diamond cluster hosting nitrogen-vacancy center, New J. Phys. **16**, 083014 (2014).

[56] L. Jiang, J. S. Hodges, J. R. Maze, P. Maurer, J. M. Taylor, D. G. Cory, P. R. Hemmer, R. L. Walsworth, A. Yacoby, A. S. Zibrov, and M. D. Lukin, Repetitive readout of a single electronic spin via quantum logic with nuclear spin ancillae, Science **326**, 267 (2009).

[57] Y. Shikano and S. Tanaka, Estimation of spin-spin interaction by weak measurement scheme, Europhys. Lett. **96**, 40002 (2011).

[58] J. Lang, B. Frank, and J. C. Halimeh, Concurrence of dynamical phase transitions at finite temperature in the fully connected transverse-field Ising model, Phys. Rev. B **97**, 174401 (2018).

[59] W. K. Wootters, Entanglement of Formation of an Arbitrary State of Two Qubits, Phys. Rev. Lett. **80**, 2245 (1998).

[60] R. Coto, M. Orszag, and V. Eremeev, Generation and protection of a maximally entangled state between many modes in an optical network with dissipation, Phys. Rev. A **93**, 062302 (2016).

[61] Olav F. Syljuåsen, Entanglement and spontaneous symmetry breaking in quantum spin models, Phys. Rev. A **68**, 060301(R) (2003).

[62] L. Robledo, L. Childress, H. Bernien, B. Hensen, P. F. A. Alkemade, and R. Hanson, High-fidelity projective read-out of a solid-state spin quantum register, Nature (London) **477**, 574 (2011).

[63] C. E. Bradley, J. Randall, M. H. Abobeih, R. C. Berrevoets, M. J. Degen, M. A. Bakker, M. Markham, D. J. Twitchen, and T. H. Taminiau, A Ten-Qubit Solid-State Spin Register with Quantum Memory up to One Minute, Phys. Rev. X **9**, 031045 (2019).

[64] A. Dréau, P. Spinicelli, J. R. Maze, J.-F. Roch, and V. Jacques, Single-Shot Readout of Multiple Nuclear Spin Qubits in Diamond under Ambient Conditions, Phys. Rev. Lett. **110**, 060502 (2013).

[65] H. P. Bartling, M. H. Abobeih, B. Pingault, M. J. Degen, S. J. H. Loenen, C. E. Bradley, J. Randall, M. Markham, D. J. Twitchen, and T. H. Taminiau, Entanglement of Spin-Pair Qubits with Intrinsic Dephasing Times Exceeding a Minute, Phys. Rev. X **12**, 011048 (2022).

[66] P. Neumann, J. Beck, M. Steiner, F. Rempp, H. Fedder, P. R. Hemmer, J. Wrachtrup, and F. Jelezko, Single-shot readout of a single nuclear spin, Science **329**, 542 (2010).

[67] H. T. Dinani, D. W. Berry, R. Gonzalez, J. R. Maze, and C. Bonato, Bayesian estimation for quantum sensing in the absence of single-shot detection, Phys. Rev. B **99**, 125413 (2019).

[68] V. Coffman, J. Kundu, and W, K. Wootters, Distributed entanglement, Phys. Rev. A **61**, 052306 (2000).